

Article

TiO₂-Embedded Biocompatible Hydrogel Production Assisted with Alginate and Polyoxometalate Polyelectrolytes for Photocatalytic Application

Renat Mansurov ^{1,*} , Irina Pavlova ², Pavel Shabadrov ¹, Anastasiya Levchenko ¹, Alexey Krinochkin ^{1,3}, Dmitry Kopchuk ^{1,3} , Igor Nikonov ^{1,3} , Anna Prokofyeva ¹, Alexander Safronov ^{1,2}  and Kirill Grzhegorzhevskii ^{1,3,*} 

¹ Ural Federal University, Mira St. 19, Ekaterinburg 620002, Russia

² Institute of Electrophysics UB RAS, Ekaterinburg 620016, Russia

³ I. Ya. Postovsky Institute of Organic Synthesis, Ural branch of RAS, 22/20 S. Kovalevskoy/Akademicheskaya St., Yekaterinburg 620990, Russia

* Correspondence: renat.mans@gmail.com (R.M.); kirillvalentinovich@urfu.ru (K.G.)

Abstract: The hybrid hydrogel materials meet important social challenges, including the photocatalytic purification of water and bio-medical applications. Here, we demonstrate two scenarios of polyacrylamide-TiO₂ (PAAm@TiO₂) composite hydrogel design using calcium alginate (Alg-Ca) or Keplerate-type polyoxometalates (POMs) {Mo₁₃₂} tuning the polymer network structure. Calcium alginate molding allowed us to produce polyacrylamide-based beads with an interpenetrating network filled with TiO₂ nanoparticles Alg-Ca@PAAm@TiO₂, demonstrating the photocatalytic activity towards the methyl orange dye bleaching. Contrastingly, in the presence of the POM, the biocompatible PAAm@TiO₂@Mo₁₃₂ composite hydrogel was produced through the photo-polymerization approach (under 365 nm UV light) using vitamin B2 as initiator. For both types of the synthesized hydrogels, the thermodynamic compatibility, swelling and photocatalytic behavior were studied. The influence of the hydrogel composition on its structure and the mesh size of its network were evaluated using the Flory–Rehner equation. The proposed synthetic strategies for the composite hydrogel production can be easily scaled up to the industrial manufacturing of the photocatalytic hydrogel beads suitable for the water treatment purposes or the biocompatible hydrogel patch for medical application.

Keywords: hydrogel; titanium dioxide; polyoxometalates; alginate; interpenetrating network; photocatalytic activities; water purification; bioapplication



check for updates

Citation: Mansurov, R.; Pavlova, I.; Shabadrov, P.; Levchenko, A.; Krinochkin, A.; Kopchuk, D.; Nikonov, I.; Prokofyeva, A.; Safronov, A.; Grzhegorzhevskii, K. TiO₂-Embedded Biocompatible Hydrogel Production Assisted with Alginate and Polyoxometalate Polyelectrolytes for Photocatalytic Application. *Inorganics* **2023**, *11*, 92. <https://doi.org/10.3390/inorganics11030092>

Academic Editor: Greta Ricarda Patzke

Received: 30 January 2023

Revised: 14 February 2023

Accepted: 17 February 2023

Published: 21 February 2023



Copyright: © 2023 by the authors. Licensee MDPI, Basel, Switzerland. This article is an open access article distributed under the terms and conditions of the Creative Commons Attribution (CC BY) license (<https://creativecommons.org/licenses/by/4.0/>).

1. Introduction

The hydrogel structure design is one of the key aspects of modern materials engineering [1]. In contrast to labor techniques of macromolecules covalent modification, the desired hydrogel properties can be reached through the different approaches, such as inorganic-organic composite production and the interpenetrating polymeric network formation [2]. The latter case can also be considered as a composite, but organic-organic, where the difference between the nature of constituent polymers gives a synergetic effect [3]. For instance, using the biocompatible non-ionogenic polyacrylamide (PAAm) matrix and polyelectrolyte alginate (Alg) macromolecules, one can combine mechanical properties of PAAm and Alg capability to immediate gel formation when contacted with Ca²⁺ cations (Alg-Ca). Such an approach opens the way to control both the gel's shape and the hydrogel penetration capability [4]. This is why this system was chosen to produce the TiO₂-embedded hydrogel beads for photocatalytic application [5].

The photoactive hydrogel production is a promising solution for the water purification process that has a crucial impact on human life across the world [6]. In line with the general green chemistry concept, the widespread toxic organic pollutants can be removed

by means of cost-effective technologies using the sunlight as renewable and inexpensive energy sources [7,8] to generate the reactive oxygen species (ROS). Titanium dioxide is a well-known semiconductor material that has been widely used for ROS production since 1972 due to the work of Fujishima and Honda, which first demonstrated its photocatalytic activity. Due to the high activity and chemical stability, TiO₂ nanoparticles destroy organic pollutants via the formation of superoxide radicals on the surface [5,9]. However, the photocatalytic application of TiO₂ is limited by the aggregation of nanoparticles in aqueous suspensions. In addition, the problem for environmental application is the difficulty of the particle extraction from the aqueous media [10]. The encapsulation of the TiO₂ nanoparticles in the hydrogel matrix is a promising approach to overcome these limits [11]. Such hydrogel matrixes demonstrate the effective swelling behavior in aqueous media followed with the high adsorption capacity of pollutants: organic dyes, pesticides, and pharmaceuticals. It is especially actual when the natural biodegradable polymers, such as polysaccharides, are used as sorbents [12,13].

Among many polysaccharides, calcium alginate-based hydrogel is the most widely used material [12,14]. At the same time, calcium alginate hydrogels have such disadvantages as low physical and mechanical properties, which, however, can be improved by combining polysaccharide matrixes with the synthetic polymers [4]. In Reference [15], interpenetrating hydrogel networks based on the calcium alginate with acrylamide were reported, which were able to withstand compression deformation of more than 90% with complete restoration of the original shape. The authors suggest that the resulting improved mechanical properties of the interpenetrating networks are due to the formation of the secondary cross-links between the acrylamide's amino groups and the alginate's carboxyl groups, as well as the ability of the ionic cross-links between alginate chains to break during the deformation and recover after unloading [15].

In contrast to labor-consuming and expensive methods [16] of PAAm-Alg composite film photo-polymerization, we used alternative approach coming from synthesis of poly-N-isopropylacrylamide hydrogel beads by using the calcium alginate as a polymerization mold [17]. We extended this simple hydrogel formation method to production of PAAm-Alg hydrogel with embedded TiO₂ nanoparticles, further denoted as Alg-Ca@PAAm@TiO₂.

The second scenario we used for composite hydrogel production is important for bio-application. To avoid any hazardous species such as ammonium persulfate or TEMED (N,N,N',N'-tetramethylethane-1,2-diamine), we used riboflavin (vitamin B2) as photoinitiator of radical polymerization under UV (365 nm) irradiation. The key component in such a system is Keplerate-type polyoxomolybdate (POM) {Mo₁₃₂}=(NH₄)₄₂[Mo^{VI}₇₂Mo^V₆₀O₃₇₂(CH₃COO)₃₀(H₂O)₇₂]·(ca.300H₂O)·(ca.10CH₃COONH₄). This POM is readily dissolved in water, forming multicharged (maximal charge 42⁻) macroanions with a diameter of 2.9 nm [18]. Taking into account the large POM's surface area (26.4 nm²) with many negatively charged centers, the {Mo₁₃₂} can be considered as the inorganic polyelectrolyte unit. Being previously associated with cationic drugs, Keplerate {Mo₁₃₂} can be embedded into PAAm hydrogel structures to provide prolonged drug release [19,20]. Moreover, if rhodamine-B is covalently bounded to the polymeric matrix, the pH-dependent Keplerate destruction will lead to arising the quenched fluorescence signal [19,21]. In the presence of TiO₂, the mechanical characteristics of photo-polymerized hydrogel can be improved [22]. Therefore, mutual presence of Keplerate {Mo₁₃₂} and the TiO₂ nanoparticles pave the way for multifunctional biocompatible hydrogel production with drug release function.

As was shown previously, {Mo₁₃₂} can trap the free radical [23], leading to a decrease in the polymerization rate. However, here we demonstrated that 15% PAAm hydrogel with the embedded TiO₂ nanoparticles, cross-linked by N,N-methylenbisacrylamide (BIS-AAm), can be produced only in the presence of {Mo₁₃₂} under neutral pH-value. In the literature, there is the protocol for photo-polymerized 16% PAAm hydrogel production in the presence of TiO₂ nanoparticles in the acidic condition [22]. The found specific behavior of PAAm@TiO₂@Mo₁₃₂ demonstrates that the use of the Keplerate POM is a powerful approach for hydrogel structure design on both the nanoscale and the macroscopic levels.

In brief, the current work shows that the two different strategies of PAAm-based hydrogel production aimed to control the photocatalytic behavior or bioinspired application by means of Alg-PAAm interpenetrating network formation or insertion of $\{Mo_{132}\}$, respectively. The produced hydrogels were examined on: photocatalytic degradation of methyl orange dye; swelling/re-swelling and thermodynamic behavior; and influence of components ratio on the hydrogel structure. Finally, the two types of hydrogel materials, Alg-Ca@PAAm@TiO₂ photocatalytic beads and biocompatible hydrogel patches PAAm@TiO₂@Mo₁₃₂, were produced.

2. Results and Discussion

2.1. Swelling Behavior and Thermodynamic Study of the Alg-Ca@PAAm@TiO₂ Beads

The scheme of the hydrogel preparation is presented in Figure 1. When PAAm content is changed from 50 to 95 wt.%, the swelling ratio of the polymeric network (α') increases for both blank Alg-Ca@PAAm and composite Alg-Ca@PAAm@TiO₂ hydrogels reaching the maximal value at 90–95 wt.% of PAAm, which is almost twice as high as the swelling ratio at the PAAm content 50 wt.% (Figure 2).

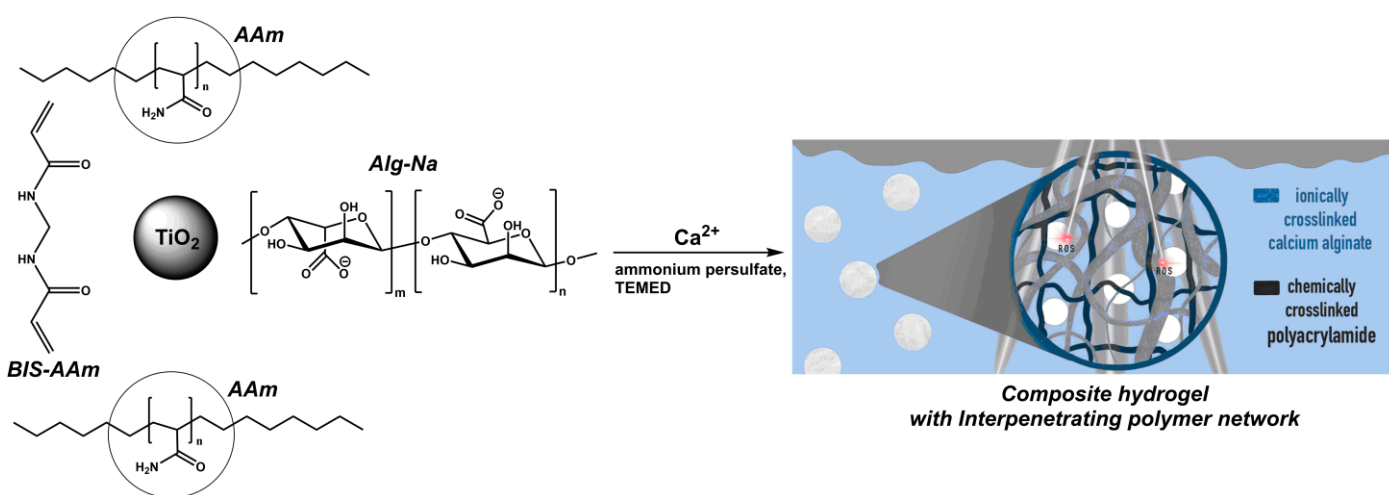


Figure 1. Illustration of the Alg-Ca@PAAm@TiO₂ hydrogel's preparation with the interpenetrating networks.

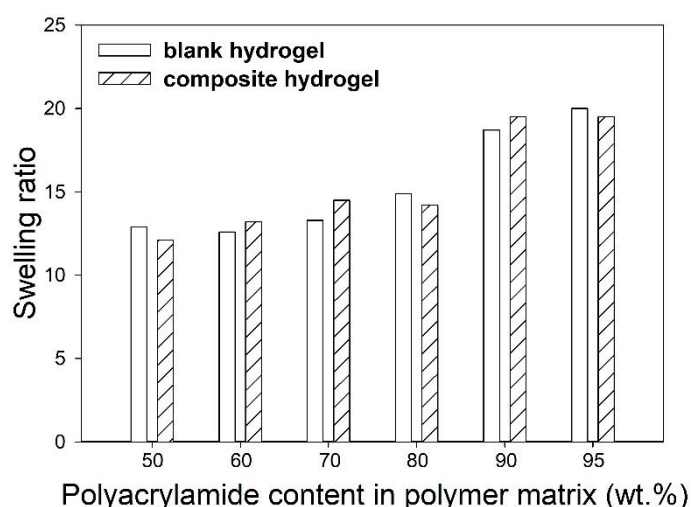


Figure 2. Swelling ratio (α') of Alg-Ca@PAAm blank hydrogel hydrogels and Alg-Ca@PAAm@TiO₂ composite hydrogel with various polyacrylamide content in polymer matrix.

Whereas the increasing content of PAAm in the interpenetrating networks Alg-Ca@PAAm strongly affects the swelling ratio, the addition of the TiO₂ nanoparticles has almost no effect on its value. Implicitly, it points out to the absence of strong interaction between the polymeric matrix and titanium dioxide. Indeed, the positive enthalpy of PAAm adhesion to the TiO₂ has been shown recently [24]. In order to evaluate the thermodynamics of the interaction in Alg-Ca@PAAm@TiO₂, we examined the enthalpy of alginate adhesion to the TiO₂ nanoparticles.

The enthalpy of an interaction among the polymer and the solid TiO₂ nanoparticles was determined for the model of binary composites in which the TiO₂ nanoparticles were embedded into the polymer matrix comprised of the linear polymeric chains. The cross-linked polymeric matrix cannot be used in this approach. Consequently, in the microcalorimetry study, the linear sodium alginate (Alg-Na) was used for the composite preparation.

To evaluate the enthalpy of an interaction among the polymer and solid filler, one should elaborate an appropriate thermochemical (Hess) cycle, which includes measurable processes containing the desired process as their combination [25]. In the case of the interaction enthalpy in the polymer/solid composite (ΔH_{int}), such a thermochemical cycle consists of the following steps: (1) wetting of the air-dry solid TiO₂ particles in liquid (ΔH_1); (2) dissolving of the polymer in the same solvent (ΔH_2); (3) mixing of the solid suspension and the polymer solution (ΔH_3); (4) dissolving of the polymer/solid composites with known TiO₂: Polymer ratio in the solvent (ΔH_4). The resulted value for the interaction enthalpy is calculated using the following equation:

$$\Delta H_{int} = \omega_1 \Delta H_1 + \omega_2 \Delta H_2 + \Delta H_3 - \Delta H_4 \quad (1)$$

where ω_1 , ω_2 are the weight fractions of the polymer and TiO₂ nanoparticles in the composite, respectively. Note that the cycle given by Equation (1) includes the dissolution of the polymer and polymeric composites and therefore it cannot be elaborated for the cross-linked polymers because the polymeric composites cannot dissolve but only swell.

As the polymer and the filler are mutually insoluble, upon the composite formation there is only one source to change the enthalpy, which is the interaction at the phase boundary. Therefore, the calculated ΔH_{int} is related to the interaction between the TiO₂ nanoparticles and the polymer chains. In Figure 3a, there is the dependence of the ΔH_3 values on the TiO₂ weight fraction in the polymeric composite. At zero weight concentration of the TiO₂ nanoparticles, the ΔH_3 value corresponds to the dissolution enthalpy of the Alg-Na as an individual polymer (ΔH_1). The wetting enthalpy of the TiO₂ nanoparticles (ΔH_2) is given by the value at the right ordinate *axis* at the TiO₂ weight fraction equals to unity, that is, $-5 \text{ J} \cdot \text{g}^{-1}$. With increasing TiO₂ weight fraction in polymeric composite, the dissolution enthalpy decreases in modulo. In accordance with Equation (1), the ΔH_{int} was calculated at a different TiO₂ content, demonstrating the absence of thermodynamic benefit from alginate adhesion onto TiO₂ nanoparticles.

Although the values of the interaction enthalpy given in Figure 3b were obtained for binary linear polymer/solid composites, we can suppose that the major features of the interaction between the polymeric chain and the solid surface of the TiO₂ nanoparticles preserve in the hydrogels as well. Because the interaction between the individual PAAm and the solid surface of the TiO₂ is also energetically unfavorable [26], the polymeric sub-chains of both the PAAm and Alg-Ca networks do not adsorb on the TiO₂ nanoparticles' surface. As a result, the TiO₂ centers remain accessible to participate in the photocatalytic process.

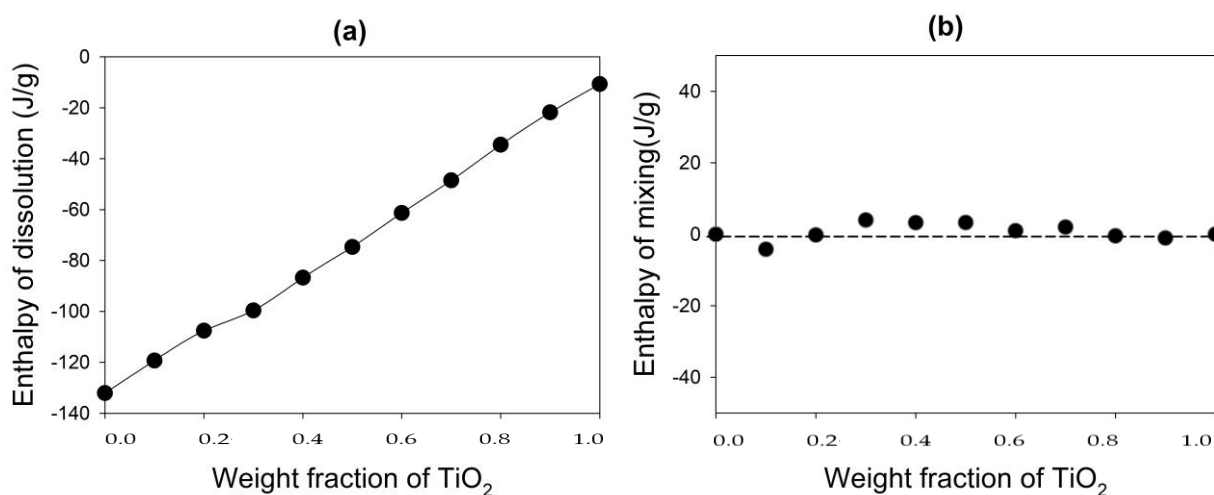


Figure 3. (a) The dissolution enthalpy of Alg-Na@TiO₂ composites and (b) the dependency of the interfacial enthalpy (ΔH_{int}) on the TiO₂ weight fraction in the Alg-Na polymer matrix.

In addition to the examination of swelling behavior tightly related to the thermodynamics of “TiO₂-Polymeric matrix” interaction, one of the major parameters for the actual application of the Alg-Ca@PAAm@TiO₂ beads is their re-swelling because of the logistic needs to transport the hydrogel in a dried state.

The possibility of the Alg-Ca@PAAm@TiO₂ hydrogel beads to restore their shape after drying was studied. This property is important for the practical application of photocatalyst hydrogels. In Figure 4, the re-swelling ability of the previously dried Alg-Ca@PAAm@TiO₂ hydrogel is shown depending on the PAAm content in the hydrogel interpenetrating networks. Re-swelling ability was calculated through the comparison of the current swelling ratio of the dried hydrogels, with one for the samples swelling immediately after preparation (see Section 3).

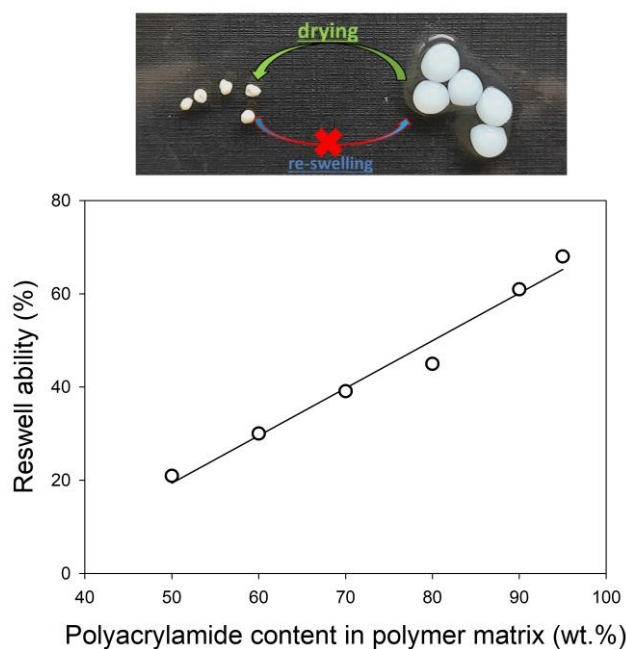


Figure 4. Re-swelling ability of the dried Alg-Ca@PAAm@TiO₂ hydrogel beads with various PAAm content. The insert presents the re-swelling process ability of the dried Alg-Ca@PAAm@TiO₂ hydrogel beads with 50 wt.% of PAAm.

In line with the swelling behavior of the Alg-Ca@PAAm@TiO₂ hydrogels, the re-swelling ability increases with increasing of the PAAm content. However, the full recovery of the swelling ratio value was not observed. For instance, the hydrogel beads sample with low PAAm content reduced its re-swelling ability almost by 80%. The reduction in the swelling ratio of dried sample can be associated with the irreversible collapse of the Alg-Ca matrix, where the polymer chains are attached to each other by multiple hydrogen bonds in addition to Ca²⁺ cations [27].

Thus, the covalently (via BIS-AAm) cross-linked PAAm network provides the re-swelling ability and prevents the UV-degradation of the Alg-Ca@PAAm@TiO₂ composite hydrogel beads. Most likely, the improved physicochemical properties of the Alg-Ca@PAAm interpenetrating networks are due to the secondary cross-link formation between amino groups of the acrylamide units in PAAm and carboxyl groups in Alg [15]. Furthermore, there is a synergetic effect, which stems both from: (i) the steric hindrance of the alginate chains, tangled with PAAm network, preventing the collapse of Alg-Ca mold; (ii) the hydrogel bead formation due to the fast gelation rate caused with the diffusion of Ca²⁺ cations from the solution into the Alg-PAAm drop.

2.2. The Photocatalytic Properties of the Alg-Ca@PAAm@TiO₂ Hydrogel Beads

In the beginning, we study the photostability of Alg-Ca@TiO₂ hydrogel beads and how the PAAm content influences that. In Figure 5, the measurements of UV-degradation degree after 5 h irradiation are presented.

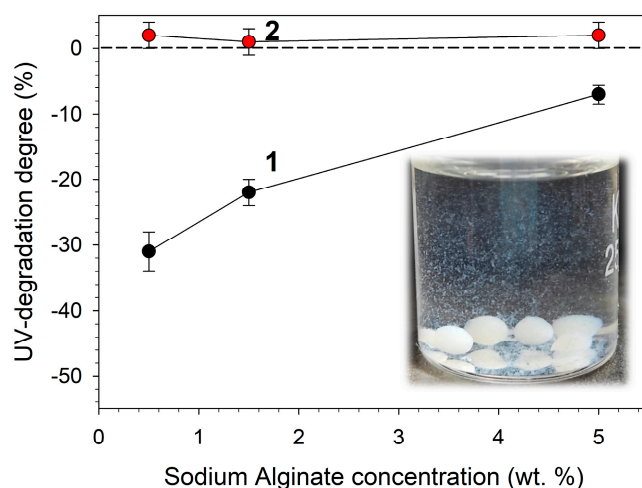


Figure 5. UV-degradation degree of the Alg-Ca hydrogel beads with (1) and without (2) embedded TiO₂ nanoparticles after 5 h of the UV irradiation depended on the initial concentration of sodium alginate. The insert presents the UV-degradation of the Alg-Ca@TiO₂ hydrogel beads produced at 0.5 wt.% of Alg-Na in aqueous solution.

The absence of measurable weight loss for blank Alg-Ca hydrogel was found. During the UV irradiation, the Alg-Ca blank hydrogels (without of the TiO₂ particles) did not degrade, regardless of initial sodium alginate (Alg-Na) concentration. To the contrary, the Alg-Ca@TiO₂ composite hydrogels were partly destroyed (see insert in Figure 5). Weight loss values are plotted as a function of the of the Alg-Na concentration, which progressively decreased with the increase in the sodium alginate content. The substantial weight loss values equal to 32 and 23% were found for hydrogel with 0.5 and 1.5% Alg-Na concentration, respectively. The higher the Alg-Na concentration, the better the UV-stability of the hydrogel. However, even moderate decomposition of the Alg-Ca@TiO₂ hydrogels under UV irradiation is not appropriate for practical application. Moreover, the measurements of the photocatalytic activity of such gels are incorrect—there is a high probability of the individual TiO₂ particles present in solution, which significantly distort the photocatalytic measurements results.

In contrast, during the 5 h under UV irradiation, the weight loss of Alg-Ca@PAAm@TiO₂ hydrogels was not observed (Figure S5, see Supporting Information). Therefore, this type of hydrogel matrix, which is more promising for the photocatalytic application, was examined towards the bleaching of methyl orange dye in the aqueous solution under UV irradiation. Furthermore, the IR spectra of swelled Alg-Ca@PAAm@TiO₂ and Alg-Ca@PAAm hydrogels (with PAAm 90% of content) after one-year storage in distilled water were measured (Figure S6, see Supporting Information). These spectra demonstrate both the stability of the hydrogel structure and that the addition of TiO₂ does not change the hydrogel structure significantly, which is in line with the thermodynamic data we obtained.

In order to uncover how the presence of the PAAm in the interpenetrating polymer networks affect the photocatalytic activity, we measured the residual concentration of the methyl orange dye in solution exposed with Alg-Ca@PAAm@TiO₂ hydrogel beads containing the different PAAm content (Figure 6a). In line with the first-order reaction kinetics model, the rate constant of methyl orange bleaching can be expressed by this equation [28]:

$$-\ln(C/C_0) = k\tau \quad (2)$$

where C_0 is the initial dye concentration; C is the residual dye concentration; τ is the duration of UV irradiation; k is an effective kinetic constant.

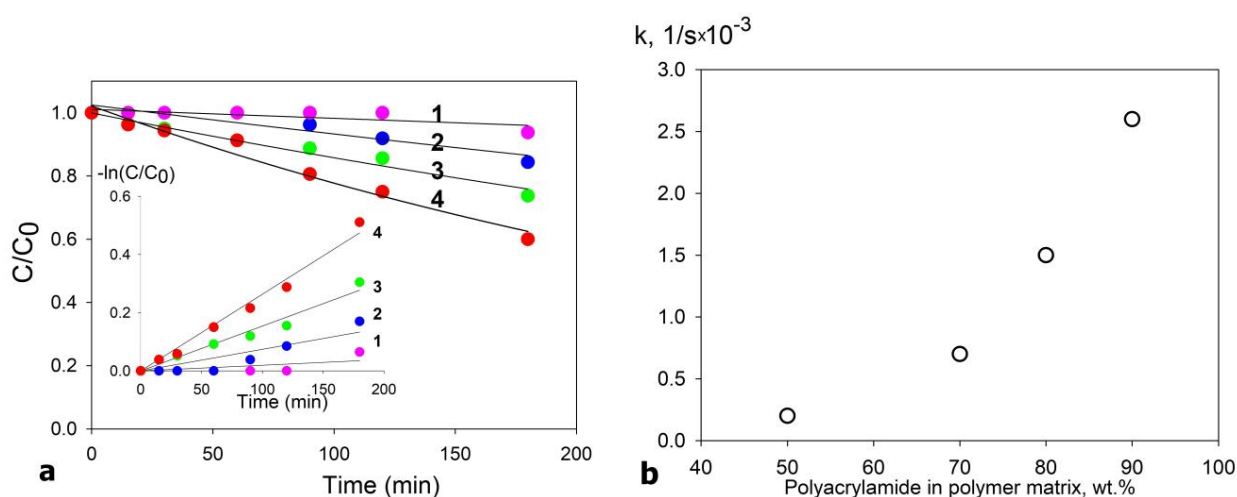


Figure 6. (a) Kinetic plots for the methyl orange dye photocatalytic decomposition by Alg-Ca@PAAm@TiO₂ hydrogel beads with various polyacrylamide content in polymer matrix: 50 wt.% (1), 70 wt.% (2), 80 wt.% (3) and 90 wt.% (4). Insert: linearization of the plots for the calculation of the effective reaction constant k according to Equation (2). (b) Dependency of the methyl orange decomposition's effective kinetic constant on the PAAm content in the Alg-Ca@PAAm@TiO₂ hydrogel beads.

As one can see, the most rapid decrease in the dye concentration was observed in the case of the Alg-Ca@PAAm@TiO₂ hydrogel beads with 90 wt.% PAAm. In the case of the hydrogel sample with 50 wt.% PAAm content, the photo-bleaching degree of the dye solution was much slower. The linear regressions by the first-order kinetics perfectly fit the experimental data, and the slope gives the value for the effective kinetic constant. For the Alg-Ca@PAAm@TiO₂ hydrogels with PAAm contents of 50, 70, 80 and 90 wt.%, the found values of k are: 0.2×10^{-3} , 0.7×10^{-3} , 1.5×10^{-3} and $2.6 \times 10^{-3} \text{ min}^{-1}$, respectively.

Among all studied Alg-Ca@PAAm@TiO₂ hydrogels, the sample with PAAm 90 wt.% demonstrated the significantly higher swelling ratio ($\alpha' = 20$), whereas the others, with 50, 70 and 80 wt.% of PAAm, possessed lower swelling ratio values: 13, 14.5 and 14, respectively (Figure 2). Consequently, the found differences in the photocatalytic behavior (Figure 6a) are not only due to the different swelling behavior. However, in general, the increasing of PAAm content in Alg-Ca@PAAm@TiO₂ leads to the exponential-like growth of the effective

kinetic constant (Figure 6b). For ROS species produced on the TiO₂ nanoparticle's surface, the diffusion coefficients are 1–3 orders smaller than those for molecules with a similar size [29]. Therefore, the photocatalytic destruction of methyl orange dye should occur near the TiO₂ surface. This process is mainly controlled by diffusion of the dye molecules from outer solution into the hydrogel and back removing of the dye's destruction product. Actually, the accessibility of photocatalyst surface is also strictly important, and in this respect, the low affinity of the alginate or PAAm polymeric chains to the TiO₂ nanoparticles is an advantage [24]. Consequently, the effective kinetic constant of methyl orange bleaching should strongly depend on the Alg-Ca@PAAm@TiO₂ hydrogel swelling ratio (Figure 6b). Interestingly, within the PAAm content range of 50–80 wt.%, the swelling ratio is kept on the same level of 13–14.5, while the effective kinetic constant grows exponential in this series. Thus, we can suppose that some intrinsic parameter of such hydrogel has an impact on the photocatalytic activity. One of the possible parameters governing the accessibility of photocatalyst surface is the disaggregation of TiO₂ nanoparticles providing homogeneous distribution across the whole hydrogel structure. Indeed, the increasing of PAAm content leads to more effective disconnection of alginate chains in the Alg-Ca network because when collapsed the Alg-Ca mold can encapsulate the TiO₂ nanoparticles, making them isolated and non-accessible.

2.3. Swelling Behavior of the PAAm@Mo₁₃₂@TiO₂ Hydrogel

The macroscopic hydrogel behavior is very sensitive to molecular structure. For instance, the increasing of the PAAm content just by 10 wt.% in Alg-Ca@PAAm@TiO₂ hydrogel leads to the effective kinetic constant of photobleaching is two times increased. Following the conception of the rational design of the hydrogel structure, we studied how the PAAm:BIS-AAm ratio, duration of an exposition under the UV light and the presence of the nanoscaled template {Mo₁₃₂} affect the mesh size of the hydrogel network (Figure 7).

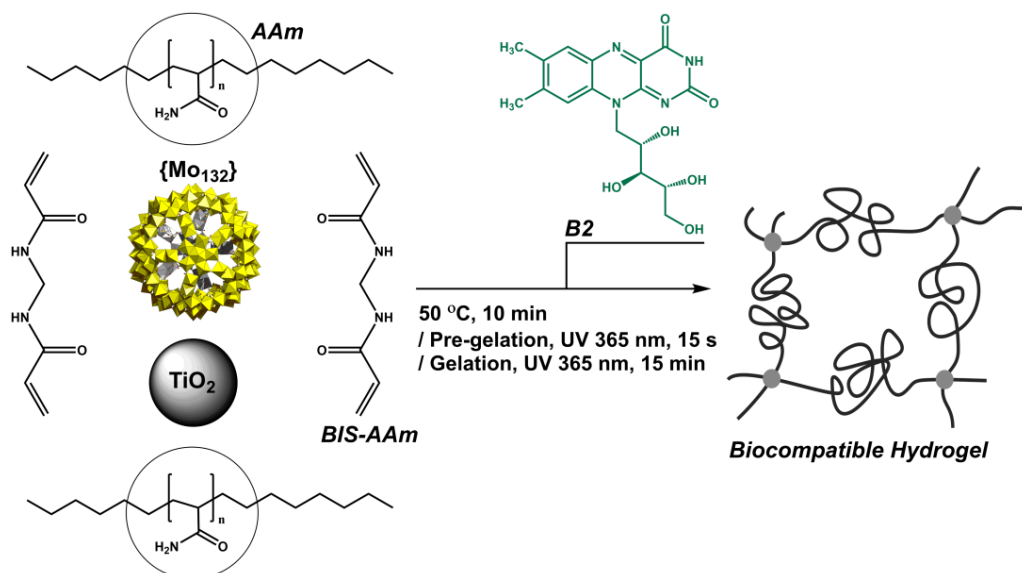


Figure 7. The scheme of the PAAm@Mo₁₃₂@TiO₂ hydrogel's synthesis via polymerization with riboflavin (vitamin B2) as the photoinitiator under the UV light irradiation. The {Mo₁₃₂} structure is represented by the coordinative oxygen polyhedra (yellow).

Unless otherwise mentioned, the basic hydrogel composition consisted of the PAAm (15 wt.%) and the BIS-AAm (0.4 wt.%). In series, we varied: the BIS-AAm concentration (0.4 and 0.8 wt.% for **Gel#1** and **Gel#2**, respectively); the time of the UV irradiation for **Gel#2** from 5 to 10 min (the latter is **Gel#3**); the concentration of the {Mo₁₃₂} (0.5 and 1.0 g·L⁻¹ for **Gel#4** and **Gel#5**, respectively); the absence and the presence of the TiO₂ nanoparticles (**Gel#6** and **Gel#7**, respectively); and the aging of the TiO₂-embedded hydrogel under

7 h of the UV irradiation (**Gel#8**). Because the addition of the TiO₂ nanoparticles into the PAAm@Mo₁₃₂ hydrogel results in the elongation of time under UV irradiation (up to 15 min) needed to complete the gelation process, we made the reference hydrogel PAAm@Mo₁₃₂, which was obtained under the same condition as PAAm@Mo₁₃₂@TiO₂; this is Gel#6. For this hydrogel series, we measured the equilibrium swelling ratio (Figure 8). As one can see, despite the double BIS-AAm concentration for Gel#2, the duration of the UV irradiation affects the swelling ratio more than BIS-AAm content as compared to Gel#1, giving the swelling ratio of 12.9, 38.3 and 13 for Gel#1, Gel#2 and Gel#3, respectively. In contrast, the exposition time under UV light was kept on the same level, but the introduction of {Mo₁₃₂} resulted in the growth of the swelling ratio from 12.9 (Gel#1) to 34.2 and 44 (for Gel#4 and Gel#5, respectively). There are two possible reasons: (i) Keplerate {Mo₁₃₂} works as optical filter decreasing the UV light flow leading to reduction in the polymerization rate; (ii) {Mo₁₃₂} can trap the free radicals produced on B2 or monomer species, leading to a decrease in the efficiency of the polymerization process. However, the increasing of the UV irradiation time up to 15 min partially reduces this effect, leading to a decrease in the swelling ratio to 18.9.

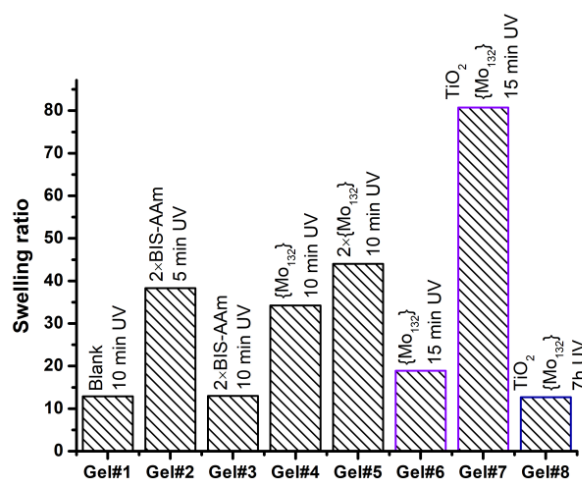


Figure 8. The swelling ratio for the PAAm (15 wt.%) hydrogels prepared under different conditions (see text for detail). Briefly, the differences between hydrogels are presented in figure. The purple frame corresponds to the hydrogel with embedded TiO₂ and reference hydrogel. The dark-blue frame corresponds to the TiO₂-embedded hydrogel after 7 h of UV irradiation.

When the TiO₂ nanoparticles were added to the PAAm/BIS-AAm/B2 mixture under neutral pH, we expected the effective polymerization under 365 nm light. Instead, the hydrogel structure was not formed; only small aggregates appeared. This result is opposite to the suggested protocol, where the only main difference in PAAm hydrogel preparation is the acidic pH [22]. It is well known that Brønsted acid/base sites (as well as Lewis acid centers) on the TiO₂ surface significantly affect the ROS generation process [30,31]. Moreover, the hydrogen bond formation led to the preferable ·OH radicals' generation on the {001} surfaces of anatase TiO₂ [32]. Therefore, the acidic environment can change the polymerization rate, leading to the hydrogel formation. However, even under neutral pH, the UV-light-assisted hydrogel formation occurred when {Mo₁₃₂} was added. The inhibition of the hydrogel formation in the PAAm/BIS-AAm/B2 mixture with the TiO₂ nanoparticles can be explained through the two hypothesizes. First, due to the fast polymerization near the TiO₂ nanoparticles, the hydrogel network does not have time to form throughout all the volume. As a result, there is no homogeneous distribution of TiO₂ in the volume and the isolated TiO₂-embedded polymeric aggregates appear. Another explanation relates to the quenching of the radical species generated from riboflavin molecules under the UV irradiation. This quenching can occur through recombination of riboflavin's or vinyl's radicals with ROS species arising from the TiO₂ surface. Therefore, being added, the

Keplerate {Mo₁₃₂} works as an optical filter decreasing the UV-light fraction absorbed by the TiO₂, which makes the polymerization more pronounced (vide infra). Interestingly, the addition of the {Mo₁₃₂} into the PAAm/BIS-AAm/B2 mixture increases the gelation time because of either the optical filter effect or free radical scavenging [23]. The gelation of the PAAm/BIS-AAm/B2 mixture with {Mo₁₃₂} and TiO₂ gives the drastic growth of the swelling ratio from 18.9 (Gel#6) to 80.7 (Gel#7). During the aging process under UV irradiation for 7 h, the swelling ratio of the Gel#7 reduced to 12.7 (Gel#8).

In accordance with the measured swelling ratio, we calculated the mesh size of the produced PAAm hydrogels. Based on the Flory–Rehner theory [33] for polymer networks, we estimated the number of monomeric residues (N_C) in the sub-chains between the crosslinks of the networks:

$$N_C = \frac{V_1 \left(0.5\alpha^{-1} - \alpha^{-\frac{1}{3}} \right)}{V_2 \left(\ln(1 - \alpha^{-1}) + \alpha^{-1} + \chi\alpha^{-2} \right)} \quad (3)$$

where the V_1 , V_2 are molar volumes of a solvent (water) and a polymer, respectively; α is the equilibrium swelling ratio; χ is the Flory–Huggins parameter for the polymer–solvent mixture. We used $V_1 = 18 \text{ cm}^3 \cdot \text{mol}^{-1}$ (water), $V_2 = 56.2 \text{ cm}^3 \cdot \text{mol}^{-1}$ (polyacrylamide) and $\chi = 0.12$ [34]. This equation gives N_C value under the assumption that polymeric sub-chains of the network are fully stretched. However, in the polyacrylamide gel, the sub-chains are statistically coiled. The mean square end-to-end distance $\langle R^2 \rangle$, between the ends of these random Gaussian coils, which corresponds to the distance between adjacent cross-links, can be calculated according to the equations:

$$N = 2N_C \quad (4)$$

$$\langle R^2 \rangle = Na^2 2 \frac{1 - \cos\theta}{1 + \cos\theta} \times \frac{1 - \cos\varphi}{1 + \cos\varphi} \quad (5)$$

where N is the number of bonds in the polymeric chain (it is two times larger than the N_C value, as it includes the bonds in monomer units and bonds between them); a is the bond length; θ is the bond angle; and φ the angle of the hindered rotation. We took $a = 0.154 \text{ nm}$ for the ordinary C–C bond, $\theta = 109.5^\circ$ and $\varphi = 120^\circ$. The calculated mesh size values (averaged R) are given in Table 1.

Table 1. The mesh size of the PAAm hydrogels calculated by means of Flory–Rehner theory.

Sample	Gel#1	Gel#2	Gel#3	Gel#4	Gel#5	Gel#6	Gel#7	Gel#8
Condition	10 min UV	×2BIS-AAm; 5 min UV	×2BIS-AAm; 10 min UV	{Mo ₁₃₂ }, 0.5 g·L ⁻¹ ; 10 min UV	{Mo ₁₃₂ }, 1.0 g·L ⁻¹ ; 10 min UV	{Mo ₁₃₂ }, 0.5 g·L ⁻¹ ; 15 min UV	{Mo ₁₃₂ }, 0.5 g·L ⁻¹ ; TiO ₂ , 1.0 g·L ⁻¹ ; 15 min UV	{Mo ₁₃₂ }, 0.5 g·L ⁻¹ ; TiO ₂ , 1.0 g·L ⁻¹ ; 15 min UV + 7 h UV
R, nm	2.5	5.6	2.2	5.0	6.3	3.0	10.7	2.1

The calculated mesh size values illustrate the above-mentioned trends. Addition of the {Mo₁₃₂} two times increases the mesh size as compared to blank hydrogel Gel#1, but elongation of an exposition under the UV light from 10 to 15 min reduces the mesh size from 5 to 3 nm (Gel#4 and Gel#6, respectively). Despite the UV irradiation for 15 min, the mesh size enlarged significantly to 10.7 nm (Gel#7). Produced Gel#7 has a homogeneous distribution of the TiO₂ nanoparticles. After aging under the UV light for 7 h, the mesh size came to value similar to Gel#1. To check whether the presence of the {Mo₁₃₂}, the TiO₂ and long-time UV irradiation influence on the PAAm network's molecular structure or not, we measured the IR spectra (Figure S7, see Supporting Information). It is clear that IR spectra of the hydrogels Gel#1, Gel#4, Gel#5 and Gel#8 (both irradiated front and nonirradiated back sides) are identical, practically. Only for Gel#8, the stretching of C–H

bond near 2925 and 2854 cm^{-1} (asymmetric and symmetric, respectively) becomes sharper and more intense.

The role of TiO_2 is not so clear. Of course, the TiO_2 nanoparticles in mixture can scatter the UV light during the gelation to obtain the hydrogel with the larger mesh size. To be scattered, UV light should interact with the TiO_2 surface. Therefore, the main question concerns whether the radical species generated onto the TiO_2 surface accelerate the polymerization or quench it through the recombination. Because the simultaneous presence of the $\{\text{Mo}_{132}\}$ and the TiO_2 leads to increase both the gelation time and the mesh size decreasing the cross-link frequency, one can assume that the TiO_2 downshifts the polymerization rate in neutral pH condition when adsorbing the UV photons. Thus, serving as optical filter, the $\{\text{Mo}_{132}\}$ prevents the TiO_2 nanoparticles from the UV light absorption.

2.4. Photostability of $\text{PAAm@Mo}_{132}@TiO_2$

To deepen understanding the role of the TiO_2 nanoparticles and to evaluate the photostability of the $\{\text{Mo}_{132}\}$ -embedded hydrogel, we studied the aging process during the long-time UV irradiation. The PAAm@Mo_{132} and $\text{PAAm@Mo}_{132}@TiO_2$ hydrogels were simultaneously exposed under the UV light (365 nm, 9 W) in two regimes: in the cell, where gel was located between two quartz windows and in the aqueous solution. In the former case, the dynamic oxygen exchange between an atmosphere and the hydrogel was absent and the swelling process was restricted by the size of the cell. In the case of an aqueous solution, both above-mentioned processes occurred in opposite fashion. In Figure 9, the comparison of the Gel#6 and Gel#7 after UV irradiation in the cell and an aqueous solution is presented. As one can see, the UV irradiation of PAAm@Mo_{132} hydrogel in both regime (7 h in the cell and 1 h in an aqueous solution, Figure 9a,e,f and Supplementary Figures S8 and S9, see Supporting Information) results in the complete bleaching of the $\{\text{Mo}_{132}\}$. This is expected behavior because the Keplerate $\{\text{Mo}_{132}\}$ can gradually decomposes in an aqueous media due to the oxidation of the Mo^{V} -centers accelerating by even the visible light irradiation [19,35,36].

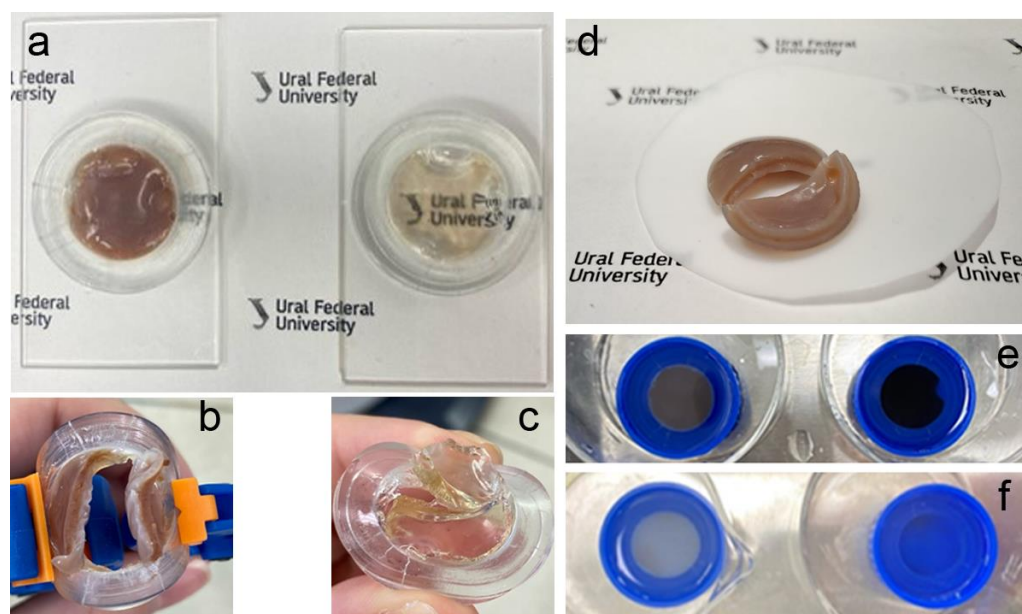


Figure 9. (a) The images of the $\text{PAAm@Mo}_{132}@TiO_2$ (left) and PAAm@Mo_{132} (right) hydrogels after UV irradiation for 7 h in the cell. (b,c) The images of the broken $\text{PAAm@Mo}_{132}@TiO_2$ and PAAm@Mo_{132} hydrogels after UV irradiation for 7 h, respectively. (d) The image of the $\text{PAAm@Mo}_{132}@TiO_2$ hydrogel (after UV irradiation for 9 h) cut in half, the back side is concaved. (e,f) The images of of the $\text{PAAm@Mo}_{132}@TiO_2$ (left) and PAAm@Mo_{132} (right) hydrogels before (e) and after (f) UV irradiation for 3 h in the aqueous solution.

In the case of the PAAm@Mo₁₃₂@TiO₂ hydrogel, the irradiation in the cell or an aqueous solution gives different results. In the aqueous solution, after an exposition under UV light for 3 h, the irradiated (front) side of the hydrogel became white colored, demonstrating the homogeneously distributed TiO₂ nanoparticles within the gel matrix (Figures S9 and S10, see Supporting Information). Irrespective of this, the nonirradiated (back) side remained the brown color, indicating the {Mo₁₃₂} preservation but with decreased concentration (Figure S10, see Supporting Information). Due to the fast decomposition of the {Mo₁₃₂} under UV light from the front side, the remained TiO₂ nanoparticles effectively scatter the light protecting the back side from the irradiation and the {Mo₁₃₂} from the decomposition, consequently. Despite the ROS generation on the TiO₂ nanoparticles under the UV light, these oxygen radicals cannot penetrate into the hydrogel network to reach the {Mo₁₃₂} on the back side owing to the short lifetime and the extremely small diffusion coefficient of the ROS [29]. In contrast, being irradiated by the UV light in the cell for 7 h, the PAAm@Mo₁₃₂@TiO₂ hydrogel became white on the back side (Figure 9b), whereas the {Mo₁₃₂} still existed on the front side, and only a very thin white layer without {Mo₁₃₂} appeared on the top of the front side. We repeated this experiment and reduced the distance between the UV LED and the cell from 25 mm to the minimal value, 15 mm. The PAAm@Mo₁₃₂@TiO₂ was irradiated for 4.5 h, kept in the dark for 17 h (to the relaxation of the intrinsic hydrogel structure) and then irradiated again for 4.5 h. After a total of 9 h of exposition under UV light, the layered structure reproduced, but the top white layer became more pronounced from the front side. Moreover, due to the long-time irradiation by UV LED placed in proximity to the cell, the hydrogel's back side was more cross-linked. When removed from the cell, the back side of Gel#8 was concaved, as compared to the front side irradiated with UV light (Figure S11c–f, see Supporting Information). Contrary to the case of the PAAm@Mo₁₃₂, the observed PAAm@Mo₁₃₂@TiO₂ hydrogel's behavior corresponds to presence of the competitive processes affecting the polymerization under UV light. In addition to the radicals' generation from the riboflavin molecules and the TiO₂ surface, as well as the {Mo₁₃₂} oxidative decomposition, one more process can exist, which is the photoinduced cascade of the electron transfer to the {Mo₁₃₂}, preventing its structure from an oxidative decomposition (Figure 10).

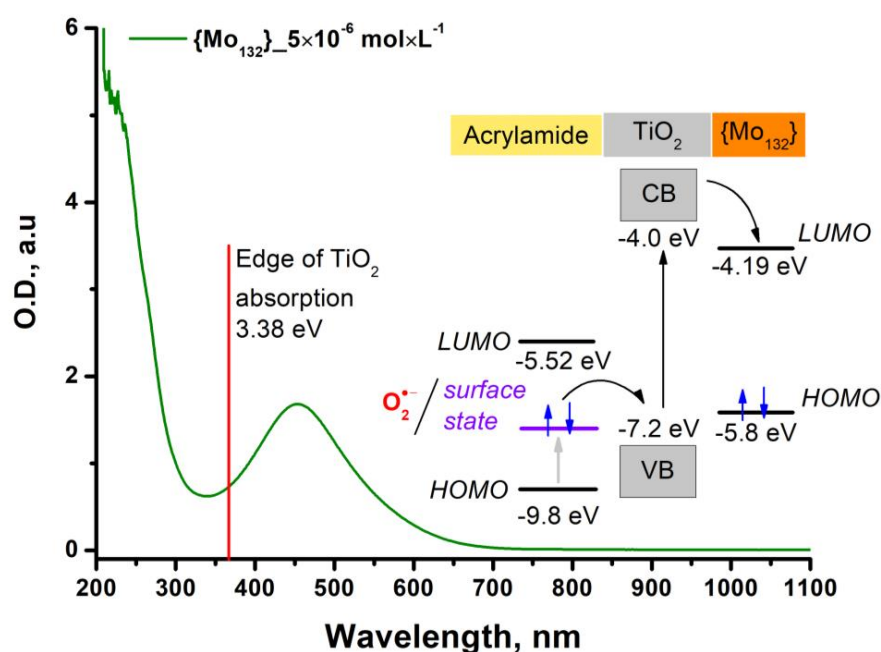


Figure 10. The UV-Vis absorption spectrum of the aqueous solution of the {Mo₁₃₂} with concentration is $5 \times 10^{-6} \text{ mol}\cdot\text{L}^{-1}$ and the energetic level diagram for the acrylamide, TiO₂ and {Mo₁₃₂} demonstrating the possible cascade of the photoinduced electron transfer. Blue arrows illustrate the electrons.

Even if we consider the random reflection of the UV light making possible some small flare of the hydrogel back side, the photon flux is incomparably bigger on the front side, where the polymerization degree should be higher. To explain the observed inversion of the cross-links frequency, we should mention that after the exposition of the liquid mixture under the UV light for 15 min to obtain the hydrogel, there is an unreacted amount of the AAm and BIS-AAm molecules. If the cross-links frequency becomes higher on the back side after 7–9 h of UV irradiation, it means that polymerization rate is faster here. Therefore, during the UV irradiation, in the hydrogel front part the preservation of {Mo₁₃₂} decreases the polymerization rate owing to the optical filter effect of the Keplerate (see absorption spectrum in Figure 10).

The presence of {Mo₁₃₂} cannot totally exclude the fact that the TiO₂ nanoparticles adsorb a small fraction of UV light across whole hydrogel. In accordance with the energetic levels diagram, the conduction band (CB) of the TiO₂ lies above the LUMO state of the {Mo₁₃₂} on the 0.19 eV [37], making possible the spontaneous electron transfer [38]. In its turn, the TiO₂ needs a sacrificial electron donor, which can be oxidized by the TiO₂ ground state (valence band, VB). The unreacted acrylamide molecules are good candidates for that, but the HOMO state of AAm is 9.8 eV, based on the Ultraviolet Photoelectron Spectroscopy [39], and the LUMO state is −5.52 eV in accordance with band gap (4.28 eV) determined by means of Tauc's plot (Figure S12, see Supporting Information). However, it is well known that the surface electronic state can be different from the bulk of the material. Furthermore, the *ab initio* calculation demonstrates that above the VB level (near 6 eV, e.g.) novel electronic states appear due to adsorption of the molecular species on the TiO₂ surface [40]. Even more, under UV light on the TiO₂ surface, the produced superoxide radicals O₂^{•−} possess the inversed HOMO-SOMO states with −5.63 eV for HOMO level. Therefore, the ad-molecules and ad-atoms can serve as the electron donors on the TiO₂ surface.

The intensification of the photoinduced cascade of the electron transfer to the {Mo₁₃₂} on the front side (where the photon flux is much higher) can explain the competition between this process and polymerization hindered by the presence of {Mo₁₃₂}. Thus, the TiO₂ behaves like a mediator of the electron transfer to {Mo₁₃₂}. This transfer occurs on the nanoparticles' surface, providing the simultaneous presence of the sacrificial donor and Keplerate at the optimal distance.

3. Materials and Methods

3.1. TiO₂ Characterization

As a photocatalyst, we used commercial titanium dioxide P25 grade purchased from Evonik. The specific surface area of it (45.2 m²/g) was determined via low-temperature equilibrium sorption of nitrogen (BET equation) using a Micromeritics TriStar 3020 vacuum sorption unit. Electron microscope photographs of the powder were obtained with a JEOL JEM 2100 transmission electron microscope (TEM) (Figure S1a, see Supporting Information). The particle size distribution was determined by the graphical analysis of the micrographs (Figure S1b, see Supporting Information). The particles were considered spherical in order to calculate the average particle size. Number average particle diameter (d_n) was 39 nm, while weighted average diameter (d_w) was 115 nm. The considerable difference between these two values indicated that the particle size distribution was broad. The phase composition of titanium dioxide was characterized via X-ray phase analysis on a Bruker D8 Discover diffractometer using CuK_α band and a graphite monochromator on a diffracted beam. Data were processed using the TOPAS 2.1 program with Ritveld's refinement of the parameters. The anatase phase, the content of which was 88 wt.%, was found to predominate (CSR size = 25 nm, lattice parameters: a = 3.786 Å, c = 9.507 Å). The rutile phase (12 wt.%) was detected in addition to the anatase phase (CSR size = 36 nm, lattice parameters: a = 4.594 Å, c = 2.959 Å). The effective band gap of titanium dioxide (3.38 eV) was determined optically [41] from the diffuse reflectance spectrum in 190–1400 nm interval

obtained using a UV-2600 Shimadzu spectrophotometer with an ISR-2600 Plus integrating sphere attachment (Figure S1c, see Supporting Information).

3.2. Hydrogel Alg-Ca@PAAm@TiO₂ Synthesis and Characterization

The synthesis of Alg-Ca@PAAm@TiO₂ composite hydrogels was carried out according to the original approach, based on the method proposed by Park and Hoffman at work [17]. The hydrogel precursors were: acrylamide (AAM, 99%, AppliChem, Darmstadt, Germany) as monomer, *N,N'*-dimethylenebisacrylamide (BIS-AAM, >98%, Merck, München, Germany) as cross-linker, sodium alginate (Alg-Na, MQ-200 grade, Merck, München, Germany) as polymerization mold, ammonium persulfate (APS, >98%, Merck, Germany) as initiator, and *N,N,N',N'*-tetramethylethane-1,2-diamine (TEMED, >99%, Merck, Germany) as catalyst. All the reagents were used as received.

First, the stock aqueous solution (gel precursor) of AAM, BIS-AAM, Alg-Na and TEMED was prepared. The weighted amount of TiO₂ was dispersed in water under ultrasound treatment using “Cole Palmer CPX 750” Ultrasonic Homogenizer (at 150 W output power for 15 min). Then, TiO₂ suspension was mixed with stock solution with vigorous stirring. The final concentration of TiO₂ suspension is 1 g·L⁻¹. The content of AAM in relation to Alg-Na varied from 50 to 95 wt.%. At the same time, the mass fraction of the {AAM + Alg-Na} mixture in the stock solution remained always the same—10 wt.%. In the reaction mixture, the final concentration of BIS-AAM and TEMED was 25 and 8.8 mM.

Further, the reaction mixture (gel precursor) was added dropwise through a needle into an aqueous solution containing 0.05 M of APS and 0.5 M of calcium chloride (Figure S2, see Supporting Information). As a result, hydrogel spherical beads instantly precipitated, forming elastic gel, Alg-Ca@PAAm@TiO₂. The resulted product was kept in a saline solution for 24 h to finalize the ion exchange and complete the acrylamide polymerization process, after the hydrogel was washed in distilled water (in static regime) for two weeks to achieve equilibrium swelling. Diameter of beads are ca. 3 mm. Synthetic procedure is presented in Figure 1.

3.3. Swelling Behavior of Alg-Ca@PAAm@TiO₂ Beads

Then, the resulting hydrogel beads were washed for two weeks in distilled water with daily water renewal to remove residual monomers and to achieve an equilibrium swelling ratio (α), which was determined gravimetrically using the following equation:

$$\alpha = \frac{m_g - m_0}{m_0} \quad (6)$$

where m_g is the mass of a swollen gel and m_0 is the mass of a gel dry residue after complete evaporation of water, which was conducted at 70 °C until a constant weight was reached.

In the case of composite gels, the swelling ratio determined according to Equation (6) gives the water content related to the combined mass of polymer and solid particles (TiO₂), although the latter do not swell. Thus, the swelling ratio of the polymeric network alone (α') was used for their characterization. It is related to the overall swelling ratio α according to the following equation:

$$\alpha' = \alpha \frac{m(\text{TiO}_2) + m_{net}}{m_{net}} \quad (7)$$

where $m(\text{TiO}_2)$ is the mass of titanium dioxide nanoparticles in the reaction mixture and m_{net} is the combined mass of monomers and cross-linker in the synthesis.

3.4. Photocatalytic Activity

In the photocatalytic activity experiments, the hydrogel samples were previously kept for 24 h in the dark in 10 mL of 3 μ M aqueous solution of methyl orange until equilibrium saturation of the hydrogel with the dye was reached. After that, the gel beads were placed in the cylindrical quartz cuvette arranged in the laboratory setup with UV irradiation (LED). The sketch of the setup is given in Figure S3 (Supporting Information). The emis-

sion spectrum of LED has maximum at 365 nm, and the light flux intensity is $16 \text{ mW}\cdot\text{cm}^{-2}$, as measured by thermopile photometer Thorlabs PM16-401. During the UV irradiation, the bleaching of the dye aqueous solution was observed due to the decomposition of the dye molecules by gel photocatalyst. At certain time intervals of irradiation, the optical density of the aqueous solution in cuvette was measured spectrophotometrically in situ by an optical fiber probe (Thorlabs Transmission Dip Probe TP22) connected to the spectrophotometer (Thorlabs CCS 100) at a wavelength of 464 nm. The measurements were carried out at 25°C under the permanent stirring of the solution with an overhead stirrer. The spectrophotometer was preliminarily calibrated for the concentration of methyl orange in an aqueous solution at a wavelength of 464 nm.

3.5. Photostability of the Hydrogel Beads Alg-Ca@PAAm@TiO₂

The photostability of the gels under UV irradiation (365 nm , light flux is $16 \text{ mW}\cdot\text{cm}^{-2}$) was determined by the gravimetric method. Since the hydrogel is a two-component system that consists of the polymer network and the bound water, the weight loss may be due to a decrease in at least one of them. The change in the mass of dried gels before and after UV irradiation characterizes the photostability of gel's polymer matrix:

$$\frac{m_0 - m_0(\text{UV})}{m_0} \times 100\% \quad (8)$$

where m_0 and $m_0(\text{UV})$ is the mass of dried gel before and after UV-irradiation, respectively. UV-irradiation of gel's samples was carried out during 5 h in thermostatically ventilated beakers with 10 mL of water.

3.6. Thermodynamic Study of the "Alginate-TiO₂" System

The enthalpy of adhesion of the alginate polymer chains to the surface of the TiO₂ particles was determined using a thermochemical cycle. Model polymer composites with the load of solid filler ranging from 0 to 100 wt.% were prepared separately as follows. A weighed portion of the TiO₂ powder was placed in this solution of sodium alginate (Alg-Na) and mechanically stirred in an agate mortar. The obtained homogeneous mixture was dried on a Teflon support to a constant weight. A weighed portion of the composite was placed in a 0.35 mL thin-walled glass ampoule and dried in a vacuum to constant weight; thereafter, the ampoule was sealed. Then, the ampoule was placed in a calorimetric cell with 5 mL of water. The thermal effects of dissolution in water of filled polymer composites and the heats of wetting of the TiO₂ particles with water were measured using a Calvet microcalorimeter of a laboratory design [42] kept at $298 \pm 0.1 \text{ K}$. During the calorimetric experiment, the ampoule was broken inside of the cell and the thermal effect was recorded. The absolute uncertainty of the calorimetric measurements, according to the electrical calibration data, was $\pm 0.02 \text{ J}$.

3.7. Hydrogel PAAm@TiO₂@Mo₁₃₂ Synthesis

The {Mo₁₃₂} crystal were produced via standard protocol [18]. Their structures were confirmed by FT-IR (Nicolet 6700, Thermo Scientific, Waltham, MA, USA) and Raman spectroscopy (Alpha 300 AR confocal Raman microscope, 633 nm laser, WiTec GmbH, St. Johann, Austria) and comparison with the literature [18,43]:

IR (ATR), {Mo₁₃₂}: $\nu(\text{OH}\cdots\text{H})$ 3398; $\nu(\text{NH in NH}_4^+)$ 3192; $\nu_{\text{as}}(\text{CH})$ 3042; $\nu_{\text{s}}(\text{CH})$ 2846; $\nu(\text{C}=\text{O})$ 1710; $\delta(\text{H}_2\text{O})$ 1616; $\nu_{\text{as}}(\text{COO}^- \text{ coordinated})$ 1546; $\delta(\text{NH}_4^+)$ 1411; $\nu_{\text{s}}(\text{COO}^- \text{ coordinated})$ 1340; 1281, $\delta_{\text{ip}}(\text{C}-\text{CH}_3, \text{ rocking})$ 1092, 1046, 1023; $\nu(\text{Mo}=\text{O})$ 964; $\nu(\text{O}-\text{Mo}-\text{O}/\text{Mo}-\text{O}-\text{Mo})$ 935, 846; $\nu(\text{Mo}-\mu_2\text{O}-\text{Mo}/\text{Mo}-\mu_3\text{O}-\text{Mo})$ 779, 704, 665 627; $\delta(\text{Mo}-\text{O}-\text{Mo})$ 558, 508; $\delta(\text{Mo}-\text{O}\mu_2-\text{Mo}/\text{Mo}-\text{O}\mu_3-\text{Mo})$ 463, 412 cm^{-1} .

Raman, {Mo₁₃₂}: $\nu_{\text{s,as}}(\text{Mo}=\text{O})$ 945m; $\nu(\text{O}-\text{Mo}-\text{O})_{\text{terminal}}$ 875s and 842(sh)m; $\nu_{\text{s}}(\text{Mo}-\text{O}-\text{Mo})$ 376s; $\delta(\text{Mo}=\text{O})$ 316m; $\delta(\text{O}-\text{Me}-\text{O})$ 215w; combination bands: 1250w, 710w.

For the hydrogel production, the following protocol was used. The stock solution (1) was prepared by dissolving acrylamide 0.75 g (Merck) and *N,N*-methylenebisacrylamide

0.02 g (Sigma-Aldrich, Burlington, NJ, USA, $\geq 99\%$) in 1.730 mL of the riboflavin (vitamin B2, Sigma-Aldrich, $\geq 98\%$) aqueous solution ($0.06 \text{ g}\cdot\text{L}^{-1}$, freshly prepared) in vial under gentle heating on the plate ($80\text{--}100 \text{ }^\circ\text{C}$ set temperature). The vial was closed with a silicon cap and covered by the aluminum foil to keep the solution in dark. To prepare the stock solution (2), 0.0025 g of $\{\text{Mo}_{132}\}$ was dissolved in 2 mL of water. After that, 0.5 mL of riboflavin solution ($0.06 \text{ g}\cdot\text{L}^{-1}$, freshly prepared) was added. In the case of TiO_2 -embedded hydrogel, the TiO_2 P25 powder 0.005 g (Evonik) was added along with $\{\text{Mo}_{132}\}$ in 2 mL of water followed with ultrasonication for 10 min.

Then 1.25 mL of stock solution (1) was kept under $50 \text{ }^\circ\text{C}$ for 10 min (in dark) and irradiated with 365 nm UV-light (18 W, LED) for 15 s to reach the pre-gelation. Immediately after that, the 1.25 mL of stock solution (2) was added and mixed with pipette. Further, mixture was transferred in the cell consisted of polyvinylchloride (PVC) ring (thickness is 3.8 mm, inner hole diameter is 19 mm) placed between two fused quartz windows. Cell was located in tight contact with two UV-LED sets (9 W per each window) and irradiated during 10 or 15 min (depended on experiment condition) while cooling with fan.

3.8. Swelling Behavior of PAAm@Mo_{132} and $\text{PAAm@TiO}_2\text{@Mo}_{132}$

Swelling behavior was studied the same way as previously described. Briefly, we kept hydrogel in 250 mL of distilled water for 10 days until reaching the constant weight. After swelling was completed, the hydrogel was dried in vacuo at $60 \text{ }^\circ\text{C}$ on rotary evaporator. The swelling ratio (α) and its corrected value (α') were calculated in accordance with Equations (6) and (7), respectively.

3.9. Photostability of PAAm@Mo_{132} and $\text{PAAm@TiO}_2\text{@Mo}_{132}$

When hydrogel was formed in the cell, the photostability was studied in two variants (Figure S4, see Supporting Information): (i) the long-time (7–9 h) irradiation in the cell only from one side with UV (365 nm) LED (9 W per side), distance is 25 mm or 15 mm; (ii) the obtained hydrogel in PVC-ring was placed in water and irradiated only from one side with UV (365 nm) LED (9 W) for 3 h.

3.10. UV-Vis Spectroscopy

The UV-Vis spectra of the aqueous solution of the acrylamide and $\{\text{Mo}_{132}\}$ were measured by the spectrometers PB-2201 (Solar Lab, Minsk, Belarus) and UV-1800 (Shimadzu, Kyoto, Japan) in the fused quartz cuvette.

4. Conclusions

In this work, the two types of PAAm-based hydrogels were produced. The hydrogel network structure was designed by means of the organic (alginate) or the inorganic (Keplerate $\{\text{Mo}_{132}\}$) polyelectrolytes. Using the Alg-Ca and TiO_2 nanoparticles, we controlled the shape and photocatalytic activity of the PAAm-based hydrogel beads, whereas the addition of $\{\text{Mo}_{132}\}$ allowed us to produce the photopolymerized biocompatible hydrogel.

In accordance with swelling behavior of the Alg-Ca@PAAm@ TiO_2 hydrogels, we found that the swelling ratio increases drastically when PAAm content reaches the 90 wt.%. To evaluate the contribution of the TiO_2 nanoparticle into the swelling behavior, the enthalpy of dissolution was measured. It clearly showed that both alginate and PAAm macromolecules have no thermodynamic benefit to interact with the TiO_2 surface, making it accessible to molecules' adsorption and ROS generation. The produced Alg-Ca@PAAm@ TiO_2 hydrogel beads demonstrated the high photocatalytic performance towards the methyl orange dye bleaching in the aqueous solution. For the Alg-Ca@PAAm@ TiO_2 hydrogels with PAAm contents of 50, 70, 80 and 90 wt.%, the found values of the effective kinetic constants k were: 0.2×10^{-3} , 0.7×10^{-3} , 1.5×10^{-3} and $2.6 \times 10^{-3} \text{ min}^{-1}$, respectively. In addition, we studied the photostability and re-swelling behavior of the Alg-Ca@PAAm@ TiO_2 hydrogel beads that is strictly important for actual photocatalytic application. As we found, the introduction of PAAm at 90 wt.% remains the re-swelling ratio on 60% from the initial

level, wherein, even at 50 wt.% of PAAm content, the photostability becomes extremely high: there is no loss of hydrogel mass during 5 h under UV irradiation, whereas for Alg-Ca@TiO₂ hydrogels the weight loss reaches 30%.

The creation of biocompatible hydrogel needs another approach. For this, we used the photopolymerization of PAAm/BIS-AAm mixture under the presence of {Mo₁₃₂}, which gave us the way to control the mesh size (2.5 and 5.0 nm without and with the {Mo₁₃₂}, respectively) and polymerization rate. Furthermore, the rational hydrogel structure designed by the {Mo₁₃₂} made possible the PAAm@Mo₁₃₂@TiO₂ hydrogel production, while the gelation did not occur in the absence of Keplerate. Varying the BIS-AAm and the {Mo₁₃₂} content as well as the irradiation regimes, we found the fast and cheap protocol for the production of TiO₂-embedded biocompatible hydrogel with tunable mesh size. Investigation of the aging process of PAAm@Mo₁₃₂@TiO₂ hydrogel under long-time UV irradiation (7–9 h) resulted in the unexpected stabilization of the {Mo₁₃₂} structure in the presence of TiO₂ nanoparticles conditioned with photoinduced electron transfer, probably.

Thus, the suggested synthetic approaches to the Alg-Ca@PAAm@TiO₂ and the PAAm@Mo₁₃₂@TiO₂ hydrogel production will be useful for smart-material design applied to photocatalytic water purification or biotechnology (such as wound dressing), respectively.

Supplementary Materials: The following supporting information can be downloaded at: <https://www.mdpi.com/article/10.3390/inorganics11030092/s1>, Figure S1: Characterization of TiO₂ nanoparticles; Figure S2: Schematic representation of the Alg-Ca@PAAm@TiO₂ hydrogel beads production; Figure S3: Experimental setup for the measurement of photocatalytic activity of hydrogel photocatalysts in methyl orange dye aqueous medium; Figure S4: Experimental setups for hydrogel irradiation. Each UV-LED module (UV-module) has 3 LED emitting light at 365 nm with 3 W per each LED giving 9 W in sum; Figure S5: The photostability of the Alg-Ca@PAAm@TiO₂ hydrogel beads with various PAAm contents; Figure S6: The IR spectra of swelled Alg-Ca@PAAm@TiO₂ and Alg-Ca@PAAm hydrogels (with PAAm 90% of content) after one-year storage in distilled water; Figure S7: The FT-IR spectra of hydrogel measured in the ATR mode. For sample code, see the manuscript; Figure S8: The images of the PAAm@Mo₁₃₂@TiO₂ (left gel) and PAAm@Mo₁₃₂ (right gel) hydrogels during the UV irradiation for 7 h in the cell; Figure S9: The images of the PAAm@Mo₁₃₂@TiO₂ (left gel) and PAAm@Mo₁₃₂ (right gel) hydrogels during the UV irradiation for 3 h in the aqueous solution; Figure S10: The images of the front (irradiated) and back (nonirradiated) sides of the PAAm@Mo₁₃₂@TiO₂ hydrogel after the UV irradiation for 3 h in the aqueous solution; Figure S11: The images of the PAAm@Mo₁₃₂@TiO₂ hydrogel after the UV irradiation; Figure S12: The Tauc's plot for UV-Vis spectrum of the acrylamide aqueous solution (7.5 g·L⁻¹).

Author Contributions: Conceptualization, R.M. and K.G.; methodology, R.M., K.G. and A.P.; analysis, A.K. and D.K.; investigation, R.M., I.P., P.S., A.L., A.P. and K.G.; resources, D.K.; writing—R.M. and K.G.; writing—review and editing, I.N., R.M., A.S., A.P. and K.G.; visualization, R.M. and K.G. All authors have read and agreed to the published version of the manuscript.

Funding: This research was supported by the Russian Scientific Foundation: Ref. # 18-73-10119-P (the synthesis of POM-embedded hydrogels) and Ministry of Science and the Higher Education of RF: Ref. # 075-15-2022-1118, dated 29 June 2022 (the investigation of properties of hydrogels).

Data Availability Statement: Data is contained within the article or Supplementary Materials.

Acknowledgments: The authors acknowledge the valuable help by A. M. Murzakayev and A. I. Medvedev for the structural characterization of titanium dioxide.

Conflicts of Interest: The authors declare no conflict of interest.

References

1. Mondal, S.; Das, S.; Nandi, A.K. A Review on Recent Advances in Polymer and Peptide Hydrogels. *Soft Matter* **2020**, *16*, 1404–1454. [[CrossRef](#)] [[PubMed](#)]
2. Guo, Y.; Bae, J.; Fang, Z.; Li, P.; Zhao, F.; Yu, G. Hydrogels and Hydrogel-Derived Materials for Energy and Water Sustainability. *Chem. Rev.* **2020**, *120*, 7642–7707. [[CrossRef](#)] [[PubMed](#)]
3. Bashir, S.; Hina, M.; Iqbal, J.; Rajpar, A.H.; Mujtaba, M.A.; Alghamdi, N.A.; Wageh, S.; Ramesh, K.; Ramesh, S. Fundamental Concepts of Hydrogels: Synthesis, Properties, and Their Applications. *Polymers* **2020**, *12*, 2702. [[CrossRef](#)] [[PubMed](#)]

4. Sun, J.Y.; Zhao, X.; Illeperuma, W.R.K.; Chaudhuri, O.; Oh, K.H.; Mooney, D.J.; Vlassak, J.J.; Suo, Z. Highly Stretchable and Tough Hydrogels. *Nature* **2012**, *489*, 133–136. [[CrossRef](#)]
5. Lei, W.; Suzuki, N.; Terashima, C.; Fujishima, A. Hydrogel Photocatalysts for Efficient Energy Conversion and Environmental Treatment. *Front. Energy* **2021**, *15*, 577–595. [[CrossRef](#)]
6. Guidetti, G.; Giuri, D.; Zanna, N.; Calvaresi, M.; Montalti, M.; Tomasini, C. Biocompatible and Light-Penetrating Hydrogels for Water Decontamination. *ACS Omega* **2018**, *3*, 8122–8128. [[CrossRef](#)] [[PubMed](#)]
7. Fagan, R.; McCormack, D.E.; Dionysiou, D.D.; Pillai, S.C. A Review of Solar and Visible Light Active TiO₂ Photocatalysis for Treating Bacteria, Cyanotoxins and Contaminants of Emerging Concern. *Mater. Sci. Semicond. Process.* **2016**, *42*, 2–14. [[CrossRef](#)]
8. Kubacka, A.; Fernández-García, M.; Colón, G. Advanced Nanoarchitectures for Solar Photocatalytic Applications. *Chem. Rev.* **2012**, *112*, 1555–1614. [[CrossRef](#)]
9. Fujishima, A.; Honda, K. Electrochemical Photolysis of Water at a Semiconductor Electrode. *Nature* **1972**, *238*, 37–38. [[CrossRef](#)]
10. Danish, M.S.S.; Estrella, L.L.; Alemáida, I.M.A.; Lisin, A.; Moiseev, N.; Ahmadi, M.; Nazari, M.; Wali, M.; Zaheb, H.; Senjyu, T. Photocatalytic Applications of Metal Oxides for Sustainable Environmental Remediation. *Metals* **2021**, *11*, 80. [[CrossRef](#)]
11. You, X.; Huang, H.; Zhang, R.; Yang, Z.; Xu, M.; Wang, X.; Yao, Y. Immobilization of TiO₂ Nanoparticles in Hydrogels Based on Poly(Methyl Acrylate) and Succinamide Acid for the Photodegradation of Organic Dyes. *Catalysts* **2021**, *11*, 613. [[CrossRef](#)]
12. Dat Mai, N.X.; Park, D.; Yoon, J.; Hur, J. Comparative Study of Hydrogel-Based Recyclable Photocatalysts. *J. Nanosci. Nanotechnol.* **2018**, *18*, 1361–1364. [[CrossRef](#)]
13. Karimi-Maleh, H.; Ayati, A.; Davoodi, R.; Tanhaei, B.; Karimi, F.; Malekmohammadi, S.; Orooji, Y.; Fu, L.; Sillanpää, M. Recent Advances in Using of Chitosan-Based Adsorbents for Removal of Pharmaceutical Contaminants: A Review. *J. Clean. Prod.* **2021**, *291*, 125880. [[CrossRef](#)]
14. Puscaselu, R.G.; Lobiuc, A.; Dimian, M.; Covasa, M. Alginate: From Food Industry to Biomedical Applications and Management of Metabolic Disorders. *Polymers* **2020**, *12*, 2417. [[CrossRef](#)] [[PubMed](#)]
15. Darnell, M.C.; Sun, J.Y.; Mehta, M.; Johnson, C.; Arany, P.R.; Suo, Z.; Mooney, D.J. Performance and Biocompatibility of Extremely Tough Alginate/Polyacrylamide Hydrogels. *Biomaterials* **2013**, *34*, 8042–8048. [[CrossRef](#)] [[PubMed](#)]
16. Wei, S.; Zhang, X.; Zhao, K.; Fu, Y.; Li, Z.; Lin, B.; Wei, J. Preparation, Characterization, and Photocatalytic Degradation Properties of Polyacrylamide/Calcium Alginate/TiO₂ Composite Film. *Polym. Compos.* **2016**, *16*, 101–113. [[CrossRef](#)]
17. Park, T.G.; Hoffman, A.S. Preparation of Large, Uniform Size Temperature-sensitive Hydrogel Beads. *J. Polym. Sci. Part A Polym. Chem.* **1992**, *30*, 505–507. [[CrossRef](#)]
18. Müller, A.; Krickemeyer, E.; Bögge, H.; Schmidtman, M.; Peters, F. Organizational Forms of Matter: An Inorganic Super Fullerene and Keplerate Based on Molybdenum Oxide. *Angew. Chemie Int. Ed.* **1999**, *37*, 3359–3363. [[CrossRef](#)]
19. Grzhegorzhevskii, K.V.; Shevtsev, N.S.; Abushaeva, A.R.; Chezganov, D.S.; Ostroushko, A.A. Prerequisites and Prospects for the Development of Novel Systems Based on the Keplerate Type Polyoxomolybdates for the Controlled Release of Drugs and Fluorescent Molecules. *Russ. Chem. Bull.* **2020**, *69*, 804–814. [[CrossRef](#)]
20. Ostroushko, A.A.; Gagarin, I.D.; Grzhegorzhevskii, K.V.; Gette, I.F.; Vlasov, D.A.; Ermoshin, A.A.; Antosyuk, O.N.; Shikhova, S.V.; Danilova, I.G. The Physicochemical Properties and Influence on Living Organisms of Nanocluster Polyoxomolybdates as Prospective Bioinspired Substances (Based on Materials from the Plenary Lecture). *J. Mol. Liq.* **2020**, *301*, 110910. [[CrossRef](#)]
21. Fazylova, V.; Shevtsev, N.; Mikhailov, S.; Kim, G.; Ostroushko, A.; Grzhegorzhevskii, K. Fundamental Aspects of Xanthene Dye Aggregation on the Surfaces of Nanocluster Polyoxometalates: H- to J-Aggregate Switching. *Chem. A Eur. J.* **2020**, *26*, 5685–5693. [[CrossRef](#)] [[PubMed](#)]
22. Zhang, W.; Yuan, Z.; Huang, L.; Kang, J.; Jiang, R.; Zhong, H. Titanium Dioxide Photocatalytic Polymerization of Acrylamide for Gel Electrophoresis (TIPPAGE) of Proteins and Structural Identification by Mass Spectrometry. *Sci. Rep.* **2016**, *6*, 1–8. [[CrossRef](#)]
23. Ostroushko, A.A.; Vazhenin, V.A.; Tonkushina, M.O. Features of Thermophotoinitiated Degradation of Nanocluster Polyoxomolybdate Mo132 and Its Polymer-Containing Composites. *Russ. J. Inorg. Chem.* **2017**, *62*, 483–488. [[CrossRef](#)]
24. Mansurov, R.R.; Pavlova, I.A.; Safronov, A.P. Adhesion of Polymer to TiO₂ Particles Decreases Photocatalytic Activity of Polyelectrolyte Hydrogel Photocatalyst. *Chem. Sel.* **2022**, *7*, e202202775. [[CrossRef](#)]
25. Shankar, A.; Safronov, A.P.; Mikhnevich, E.A.; Beketov, I.V.; Kurlyandskaya, G.V. Ferrogels Based on Entrapped Metallic Iron Nanoparticles in a Polyacrylamide Network: Extended Derjaguin–Landau–Verwey–Overbeek Consideration, Interfacial Interactions and Magnetodeformation. *Soft Matter* **2017**, *13*, 3359–3372. [[CrossRef](#)] [[PubMed](#)]
26. Mansurov, R.R.; Zverev, V.S.; Safronov, A.P. Dynamics of Diffusion-Limited Photocatalytic Degradation of Dye by Polymeric Hydrogel with Embedded TiO₂ Nanoparticles. *J. Catal.* **2021**, *406*, 9–18. [[CrossRef](#)]
27. Serrano-Aroca, Á.; Ruiz-Pividal, J.F.; Llorens-Gámez, M. Enhancement of Water Diffusion and Compression Performance of Crosslinked Alginate Films with a Minuscule Amount of Graphene Oxide. *Sci. Rep.* **2017**, *7*, 11684. [[CrossRef](#)]
28. Ong, S.A.; Min, O.M.; Ho, L.N.; Wong, Y.S. Comparative Study on Photocatalytic Degradation of Mono Azo Dye Acid Orange 7 and Methyl Orange under Solar Light Irradiation. *Water. Air. Soil Pollut.* **2012**, *223*, 5483–5493. [[CrossRef](#)]
29. Okuda, M.; Tsuruta, T.; Katayama, K. Lifetime and Diffusion Coefficient of Active Oxygen Species Generated in TiO₂ Sol Solutions. *Phys. Chem. Chem. Phys.* **2009**, *11*, 2287–2292. [[CrossRef](#)]
30. Ding, L.; Li, M.; Zhao, Y.; Zhang, H.; Shang, J.; Zhong, J.; Sheng, H.; Chen, C.; Zhao, J. The Vital Role of Surface Brønsted Acid/Base Sites for the Photocatalytic Formation of Free ·OH Radicals. *Appl. Catal. B Environ.* **2020**, *266*, 118634. [[CrossRef](#)]

31. Nakamura, R.; Okamura, T.; Ohashi, N.; Imanishi, A.; Nakato, Y. Molecular Mechanisms of Photoinduced Oxygen Evolution, PL Emission, and Surface Roughening at Atomically Smooth (110) and (100) n-TiO₂ (Rutile) Surfaces in Aqueous Acidic Solutions. *J. Am. Chem. Soc.* **2005**, *127*, 12975–12983. [[CrossRef](#)]
32. Zhang, H.; Zhou, P.; Chen, Z.; Song, W.; Ji, H.; Ma, W.; Chen, C.; Zhao, J. Hydrogen-Bond Bridged Water Oxidation on {001} Surfaces of Anatase TiO₂. *J. Phys. Chem. C* **2017**, *121*, 2251–2257. [[CrossRef](#)]
33. Quesada-Pérez, M.; Maroto-Centeno, J.A.; Forcada, J.; Hidalgo-Alvarez, R. Gel Swelling Theories: The Classical Formalism and Recent Approaches. *Soft Matter* **2011**, *7*, 10536–10547. [[CrossRef](#)]
34. Kurlyandskaya, G.V.; Svalov, A.V.; Burgoa Beitia, A.; Safronov, A.P.; Blyakhman, F.A.; Fernández, E.; Beketov, I.V. Magnetoimpedance Biosensor Prototype for Ferrogel Detection. *J. Magn. Magn. Mater.* **2017**, *441*, 650–655. [[CrossRef](#)]
35. Ostroushko, A.A.; Tonkushina, M.O. Destruction of Porous Spherical Mo132 Nanocluster Polyoxometallate of Keplerate Type in Aqueous Solutions. *Russ. J. Phys. Chem. A* **2016**, *90*, 436–442. [[CrossRef](#)]
36. Tereshchenko, K.A.; Shiyan, D.A.; Grzhegorzhevskii, K.V.; Lyulinskaya, Y.L.; Okhotnikov, G.O.; Ulitin, N.V.; Khursan, S.L.; Abramov, P.A. Kinetics and Mechanism of a Self-Oscillation Reaction of Keplerate-Type Polyoxomolibdate Degradation in an Aqueous Solution. *J. Struct. Chem.* **2022**, *63*, 2004–2019. [[CrossRef](#)]
37. Xu, S.; Wang, Y.; Zhao, Y.; Chen, W.; Wang, J.; He, L.; Su, Z.; Wang, E.; Kang, Z. Keplerate-Type Polyoxometalate/Semiconductor Composite Electrodes with Light-Enhanced Conductivity towards Highly Efficient Photoelectronic Devices. *J. Mater. Chem. A* **2016**, *4*, 14025–14032. [[CrossRef](#)]
38. Turo, M.J.; Chen, L.; Moore, C.E.; Schimpf, A.M. Co²⁺-Linked [NaP5W30O110]14-: A Redox-Active Metal Oxide Framework with High Electron Density. *J. Am. Chem. Soc.* **2019**, *141*, 4553–4557. [[CrossRef](#)]
39. Evangelisti, L.; Melandri, S.; Negri, F.; Coreno, M.; Prince, K.C.; Maris, A. UPS, XPS, NEXAFS and Computational Investigation of Acrylamide Monomer. *Photochem* **2022**, *2*, 463–478. [[CrossRef](#)]
40. Martsinovich, N.; Jones, D.R.; Troisi, A. Electronic Structure of TiO₂ Surfaces and Effect of Molecular Adsorbates Using Different DFT Implementations. *J. Phys. Chem. C* **2010**, *114*, 22659–22670. [[CrossRef](#)]
41. López, R.; Gómez, R. Band-Gap Energy Estimation from Diffuse Reflectance Measurements on Sol-Gel and Commercial TiO₂: A Comparative Study. *J. Sol-Gel Sci. Technol.* **2012**, *61*, 1–7. [[CrossRef](#)]
42. Safronov, A.P.; Istomina, A.S.; Terziyan, T.V.; Polyakova, Y.I.; Beketov, I.V. Influence of Interfacial Adhesion and the Nonequilibrium Glassy Structure of a Polymer on the Enthalpy of Mixing of Polystyrene-Based Filled Composites. *Polym. Sci. Ser. A* **2012**, *54*, 214–223. [[CrossRef](#)]
43. Grzhegorzhevskii, K.V.; Zelenovskiy, P.S.; Koryakova, O.V.; Ostroushko, A.A. Thermal Destruction of Giant Polyoxometalate Nanoclusters: A Vibrational Spectroscopy Study. *Inorg. Chim. Acta* **2019**, *489*, 287–300. [[CrossRef](#)]

Disclaimer/Publisher's Note: The statements, opinions and data contained in all publications are solely those of the individual author(s) and contributor(s) and not of MDPI and/or the editor(s). MDPI and/or the editor(s) disclaim responsibility for any injury to people or property resulting from any ideas, methods, instructions or products referred to in the content.